Author Manuscript

Author Manuscript

Author Manuscript

Author Manuscript

HHS Public Access

Author manuscript

Contrast Media Mol Imaging. Author manuscript; available in PMC 2020 January 05.

Published in final edited form as:

Contrast Media Mol Imaging. 2011 ; 6(5): 370–377. doi:10.1002/cmmi.439.

Gold nanocages as contrast agents for photoacoustic imaging†

Weiyang Li[a], **Paige K. Brown**[a], **Lihong V. Wang**[a], **Younan Xia**[a,*]

[a]Department of Biomedical Engineering, Washington University in St Louis, St Louis, MO 63130, USA

Abstract

Gold nanoparticles with tunable absorption and scattering properties have been developed as contrast agents for various optical imaging techniques. As a hybrid modality that combines the merits of both optical and ultrasonic imaging, photoacoustic (PA) imaging also benefits from the use of these nanoparticles to greatly enhance the contrast for visualization of structures and biomarkers in biological tissues. Gold nanocages characterized by hollow interiors, ultrathin and porous walls are of particular interest for *in vivo* PA imaging because of their compact sizes, bio-inertness and well-defined surface chemistry, as well as their strong and highly wavelength-tunable optical absorption in the near-infrared (NIR) optical window of soft tissues. This review discusses the application of gold nanocages as a new class of contrast agents for PA imaging in the context of cancer diagnosis.

Keywords

gold nanocages; photoacoustic tomography; photoacoustic microscopy; contrast agent; localized surface plasmon resonance

1. INTRODUCTION

For early diagnosis of malignant tumors and other pathologies, there remains a strong need for a noninvasive, safe and economic imaging technique that uses nonradioactive contrast agents and provides a means for precise image-guided resection of diseased tissue. Optical imaging modalities are nonionizing and cost-effective, and they can provide excellent imaging contrast based on interactions between light and different tissue components, predominantly by either absorption or scattering events (1). It is known that optical absorption can be harnessed for functional imaging to reveal, for example, cancer hallmarks including angiogenesis and hypermetaboilsm due to the different absorption properties of endogenous species and exogenous contrast agents (2). Although optical imaging techniques can provide impressive optical-based contrast, penetration depth of unscattered photons is inherently limited by the strong scattering of light in biological tissues. As an imaging modality that can overcome this limitation and provide relatively high and scalable spatial

†This article is published in Contrast Media and Molecular Imaging as part of the special issue on Photoacoustic Imaging, edited by Dr. Gregory Lanza, Department of Medicine, Washington University Medical Hospital.

*Correspondence to: Y. Xia, Department of Biomedical Engineering, Washington University in St Louis, St Louis, MO 63130, USA. xia@biomed.wustl.edu.

Author Manuscript Author Manuscript Author Manuscript Author Manuscript

resolution, ultrasonography seems to be a viable alternative but lacks the molecular and functional information that optical absorption provides (3). Photoacoustic (PA) imaging is a hybrid imaging modality that combines the beneficial aspects of both optical and ultrasonic imaging techniques (4–6). It not only takes advantage of the strong optical absorption contrast associated with optical imaging but also offers high ultrasonic spatial resolution. The maximum imaging depth of PA imaging in biological tissues can be pushed up to 50 mm by using diffusive photons (7–9). In contrast, purely optical imaging methods cannot provide high spatial resolution beyond one optical transport mean free path (~1 mm) (1,10).

Although the PA signal is sensitive to endogenous molecules such as hemoglobin or melanin, exogenous contrast agents are still needed for additional signal enhancement and thus precise visualization and delineation of different structures in biological tissues. Nanoparticles with strong optical absorption have been investigated as contrast agents, especially those based on gold (Au) and characterized by different morphologies (11). Gold nanoparticles can strongly absorb and scatter light at specific wavelengths, in a phenomenon commonly known as localized surface plasmon resonance (LSPR). For *in vivo* optical imaging techniques, in order to maximize the penetration depth in biological tissues, the LSPR peaks of nanoparticles to be used as contrast agents have to be tuned to the near-infrared (NIR) region ranging from 700 to 900 nm, in the so-called optical window where the attenuation of light by blood and soft tissues is relatively low (12). This requirement cannot be satisfied with the conventional Au colloids characterized by a solid and a spherical (more or less) shape. To solve this problem, both Au nanorods and nanoshells have been developed by a number of research groups (13,14). Our group has also developed a novel class of Au-based nanostructures – Au nanocages (AuNCs) characterized by a single-crystal structure, hollow interiors, ultrathin and porous walls (15). The LSPR peaks of AuNCs can be easily and precisely tuned to any wavelength in the NIR region by controlling the size and/or wall thickness, making them ideal candidates of contrast agents for PA imaging. Other significant features of AuNCs as contrast agents reside in their much larger absorption cross sections (almost five orders of magnitude greater than those of conventional organic dyes), the low cytotoxicity of Au, as well as their ability to be easily bioconjugated with tumor-specific ligands (16–18).

In this review, we will first give a brief overview of the synthesis and optical properties of AuNCs, and then present a simple method based on PA imaging for measuring the absorption cross sections of Au-based nanostructures with different morphologies including nanocages, nanorods and nanospheres. Finally, we will highlight several demonstrations related to the use of AuNCs as contrast agents for *in vivo* PA imaging of different components in biological tissues, such as cerebral cortex, lymph nodes and melanoma tumors.

2. SYNTHESIS AND OPTICAL PROPERTIES OF GOLD NANOCAGES

In the presence of Ag solid, a Au salt, for example, $HAuCl_4$, can be reduced to generate Au atoms through the galvanic replacement reaction in an aqueous solution because of the difference in electrochemical potential between Ag/Ag^+ (0.80V) and $Au/AuCl_4^-$ (1.00V) (19). The reaction can be described as the following:

Author Manuscript Author Manuscript Author Manuscript Author Manuscript

$$3Ag(s) + AuCl_4^-(aq) \rightarrow Au(s) + 3Ag^+(aq) + 4Cl^-(aq) \quad (1)$$

Silver nanostructures with all morphologies can serve as templates for nucleation and growth of Au, imparting their shapes to the resultant nanostructures. In the case of AuNCs, they are typically synthesized by templating against Ag nanocubes. Figure 1(A, B) shows scanning electron microscopy (SEM) images of Ag nanocubes and the resultant AuNCs, respectively, and the insets display their corresponding transmission electron microscopy (TEM) images. In order to generate AuNCs with high uniformity in terms of both sizes and shapes, one needs to start with Ag nanocubes narrowly distributed in size. We and others have developed a number of methods for the synthesis of Ag nanocubes, and their edge lengths could be readily controlled from 30 to 200 nm by adjusting the reaction parameters (19–23). Among these methods, the protocol based on polyol reduction has proven to be a facile route to high-quality Ag nanocubes in large quantities, in which ethylene glycol acts as both the solvent and source of reducing agent, and $AgNO_3$ or CF_3COOAg serves as a precursor to elemental Ag. The growth process is assisted with poly(vinyl pyrrolidone) (PVP), a capping agent capable of selectively binding to the {100} facets. Meanwhile, the addition of a trace amount of NaHS and/or Cl^- ions into the reaction allowed rapid nucleation of single-crystal seeds and elimination of the twinned seeds due to oxidative etching, ensuring the formation of single-crystal Ag nanocubes.

With respect to the synthesis of AuNCs, an aqueous solution of $HAuCl_4$ is typically titrated into an aqueous suspension of Ag nanocubes. The temperature of the reaction is maintained at 100°C in order to ensure an epitaxial growth for the Au atoms on the Ag nanocubes by avoiding the precipitation of AgCl (the solubility product, K_{sp}, is 1×10^{-6} at 100°C vs 1.56×10^{-10} at room temperature) during galvanic replacement. When the reaction is stopped and cooled down to room temperature, the AgCl will precipitate out, but it can be dissolved by saturated NaCl solution through the formation of a soluble coordination complex with chloride. As a result, this by-product can be removed (together with the supernatant) from the AuNCs by centrifugation (24). According to a thorough mechanistic study by our group (19), the transformation from Ag nanocubes with sharp corners to AuNCs proceeds through the following steps: (i) Ag dissolution is initiated by pitting at a specific spot with high surface energy on the surface of a Ag nanocube (e.g., point defect or hole in the capping layer); (ii) more Ag from the interior of the cube is dissolved through the initial pinhole while a layer of Au is deposited on the surface of the cube, forming a Au–Ag nanobox through a combination of galvanic replacement and Au-Ag alloying; and (iii) pores are generated on the walls of the nanobox through a dealloying process, forming a highly porous structure known as nanocage. When the Ag nanocubes are truncated at corners, the pores will be preferentially generated at all the corners (25). In either case, the reaction process can be monitored by taking UV–vis spectra of aliquots sampled from the reaction solution at different times. Figure 1(C) shows the extinction spectra recorded from samples obtained by titrating Ag nanocubes with different volumes of $HAuCl_4$ solution, corresponding to the different stages described above from Ag nanocubes to AuNCs. The LSPR peaks of the samples shifted from the visible to the NIR region as more $HAuCl_4$ was added, indicating the easiness and precision in tuning the LSPR properties.

Author Manuscript Author Manuscript Author Manuscript Author Manuscript

3. MEASURING THE ABSORPTION CROSS SECTIONS OF GOLD NANOCAGES BY PA IMAGING

The extinction peak, also known as the LSPR of plasmonic nanostructures, consists of two components, absorption and scattering. Since the relative magnitude of light absorbed or scattered can be quantified by optical cross sections, the overall extinction cross section (σ_e) can also be divided into two parts, the absorption and the scattering cross sections (σ_a and σ_s, respectively). These two components are highly dependent on the size, shape, structure (solid vs hollow), and surroundings of the nanostructures. By tailoring these parameters, one can readily manipulate one of the two components for specific optical applications. For example, plasmonic nanostructures with relatively large σ_a can serve as contrast agents for PA imaging, while those with large σ_s is better-suited for optical coherence tomography (OCT) and dark-field optical microscopy (1). Therefore, it is necessary to know the relative contributions of σ_a and σ_s in order to optimize them for different applications.

Usually, σ_e can be calculated using Beer-Lambert Law according to the extinction spectra recorded using a UV–vis–NIR spectrometer (26). In order to separate the contributions of σ_a and σ_s to σ_e, theoretical calculations such as Mie theory (for spherical particles) and the discrete-dipole approximation (DDA, for particles with arbitrary shape) are usually employed (27,28). Although both theories can provide the expected σ_a and σ_s, it is still relatively difficult to experimentally measure these two parameters. We recently developed a simple approach that can measure σ_a of Au nanostructures with various morphologies (e.g. nanospheres, nanocages, nanorods) based on PA imaging (29). Since the PA signal is generated as a result of the optical absorption of a material, the signal amplitude should be proportional to the absorption coefficient (μ_a) of the material within a certain concentration range (30). Based on this principle, we first converted the PA signal to μ_a by benchmarking against a linear calibration curve (PA signal vs μ_a) derived from a set of aqueous solutions of an organic dye with a known σ_a, (e.g. methylene blue) at different concentrations. Then, we calculated σ_a by dividing the μ_a by the corresponding concentration of the sample tested. Since σ_e can be obtained from the extinction spectra, σ_s can now be easily derived from the equation $\sigma_e = \sigma_a + \sigma_s$.

Figure 2 (top) shows an experimental setup of the PA imaging system for the optical measurements. Three Tygon^R tubes were filled with aqueous suspensions of Au nanostructures or aqueous solutions of methylene blue, and they were embedded in an optically scattering medium which can prevent direct illumination of the sample by light. The light traveled down through an optical condenser and was focused on the samples in the tubes. When the sample was irradiated by the light scattered from the laser, some light was absorbed and converted into heat, generating ultrasonic waves, which were collected by a single-element 5 MHz ultrasound transducer placed inside the condenser. The spatial resolutions of the PA imaging system were 138 μm in the axial direction and 490 μm in the transverse direction. One-dimensional (A-scan) depth-resolved images (along the *z*-direction) could be obtained by measuring the arrival times of the PA signals, and two-dimensional PA images were acquired by scanning along the *x*-direction. Figure 2 (bottom) shows a typical depth-resolved, B-scan PA image of suspensions of AuNCs (edge length ~45

Author Manuscript Author Manuscript Author Manuscript Author Manuscript

nm) at three concentrations of 0.13, 0.07 and 0.03 nM. The PA signals decreased with decreasing concentration of nanocages, indicating the proportional relationship between the PA signal and the concentration of particles.

Table 1 shows a comparison of the optical cross sections of Au nanostructures with different sizes and morphologies obtained by PA imaging and theoretical calculation. DDA was used for the calculation of AuNCs and nanorods, while the Mie theory was applied for the calculation of Au nanospheres. It can be seen that each type of Au nanostructures has its own characteristic absorption to extinction ratio (σ_a/σ_e), which agrees well with the calculated theoretical value. The discrepancies in the absolute value of σ_a and σ_e of AuNCs between experimental and theoretical results might be due to the variations in shape, wall thickness, and pore size of the nanocages. In addition, the σ_a/σ_e ratio for AuNCs with a smaller size (0.94) was higher than that of AuNCs with a larger size (0.82), while the absolute value of σ_a of large AuNCs (5.96×10^{-15} m^2) was almost two times higher than that of small AuNCs (3.05×10^{-15} m^2). The σ_a values of nanocages were much higher than those of nanorods (1.87×10^{-15} m^2), indicating that the nanocages are better candidates as contrast agents for optical imaging.

4. GOLD NANOCAGES FOR PA IMAGING OF CEREBRAL CORTEX

Photoacoustic imaging has been successfully applied to the high-resolution visualization of structures in biological tissues at various depths, and has been demonstrated to be especially useful in imaging the cerebral cortex of small animals (3,31–33). It is known that nanoparticles can accumulate in a tumor or inflamed tissue via a passive targeting mechanism referred to as the enhanced permeability and retention (EPR) effect associated with the leaky vasculature and the dysfunctional lymphatic system of a tumor. This special feature is particularly useful for brain tumor detection because these particles could be denied access to the healthy vessels in the brain by the blood–brain barrier. Therefore, cancerous lesions in the brain could be imaged with accuracy due to the permeable or leaky state of surrounding blood vessels which allows for accumulation of nanoparticles and thus provides enhanced contrast. Gold nanoshells, a new type of optical tunable nanoparticles, were tested by Wang's group as an exogenous contrast agent for visualization of vasculature in the rat brain (34). Compared with Au nanoshells, AuNCs with more compact sizes (<50 nm for AuNCs vs >100 nm for Au nanoshells) and their larger optical absorption cross section should be better suited for *in vivo* PA imaging.

In a recent study, AuNCs have been successfully demonstrated as an intravascular contrast agent for PA imaging of a rat's cerebral cortex (35). Figure 3(A) shows an *ex vivo* study that compared the PA signals generated by pure rat blood and by a mixture of AuNC-rat blood (at a concentration of 0.8×10^9 nanocages per gram of body weight). It can be observed that the PA signal amplitudes of the AuNC–blood mixture were increased by 85–106% over those of pure blood across a range of laser wavelengths from 764 to 824 nm. An *in vivo* experiment was conducted by sequentially injecting AuNCs functionalized with polyethylene glycol (PEG) into the circulatory system of a rat in three administrations of 0.8×10^9 nanocages/g body weight. PA imaging of the rat's brain was performed immediately prior to the first injection and up to 5 h after the final injection. Figure 3(B and C) shows the

Author Manuscript Author Manuscript Author Manuscript Author Manuscript

PA images of a rat's cerebral cortex before the injection of AuNCs and about 2 h after the final injection of AuNCs, respectively. The PA images clearly demonstrated that the rat brain's vasculature could be imaged with greater clarity and enhanced contrast using AuNCs as contrast agents. By calculating the optical absorption of all PA images taken at different time points after the administration of AuNCs, it was found that the enhancement of blood absorption had a peak value of 81% over the intrinsic contrast at about 2 h after the final injection, which surpasses the 63% enhancement when Au nanoshells were used at similar doses (34). According to DDA simulations for the extinction properties of nanocages and nanoshells, although the Au nanoshells generally have greater extinction coefficient overall, AuNCs have significantly greater absorption cross section and absorption-to-scattering ratio around 800 nm. Therefore, the high tendency of AuNCs to absorb vs scatter light at their LSPR wavelengths makes them more attractive as contrast agents for an absorption-based imaging modality, such as PA imaging, than nanostructures of other morphologies. This improvement in contrast using AuNCs allows for more detailed and precise imaging of deep tissue vasculature and other structures, and thus more accurate detection of cancerous tissues in early states.

5. GOLD NANOCAGES FOR PA MAPPING OF SENTINEL LYMPH NODES

In addition to their application as an intravascular contrast agent, AuNCs can be used for cancer diagnosis, for example, in the context of sentinel lymph node (SLN) mapping (36). Breast cancer commonly spreads to the axillary lymph nodes, and metastasis to these lymph nodes is considered to be one of the most important predictors of prognosis. Sentinel lymph node biopsy (SLNB) has emerged as the preferred method for axillary lymph node staging (37). The first lymph node receiving drainage from the tumor is defined as the SLN and is most likely to be positive for metastases. Before a biopsy can be taken for staging purposes, SLN must be identified. Current methods for SLN mapping usually use a blue dye (e.g. isosulfan blue or methylene blue) or radioactive colloids (e.g. technetium-99 or ^{99}mTc) (38,39). However, these approaches require either invasive techniques to visualize the blue stain or specialized facilities to deal with potentially hazardous radioactive components (40,41). Therefore, a technique which can map SLN without surgery or radioactivity is highly desirable.

Many imaging modalities, such as fluorescence imaging and magnetic resonance imaging (MRI), have been explored for noninvasive and nonionizing SLN mapping (42,43). As for fluorescence imaging, fluorescent beads or quantum dots have been used as optical lymph node tracers (41,44). However, the fluorescence-based imaging system has poor spatial resolution beyond one optical transport mean free path (~1 mm), which is not sufficient to clearly reveal the location of the SLN (the top surface of SLN in humans locates at an average depth of 12 ± 5 mm underneath the skin). Additionally, the high toxicity of quantum dots limits their application in clinical use (45). With respect to MRI, even though it can offer much better spatial resolution than optical imaging, its high cost and relatively low sensitivity are still major issues for practical applications. In comparison, a combination of AuNCs and PA imaging can provide high sensitivity, high spatial resolution and excellent imaging depth for SLN mapping at low cost, and therefore holds great potential to improve the techniques for axillary lymph node staging of breast cancer.

Author Manuscript Author Manuscript Author Manuscript Author Manuscript

Figure 4(A) shows a PA image of the axillary region of a rat before the injection of AuNCs (as a control experiment), revealing the vasculature within ~3mm below the skin surface. Figure 4(B) shows a PA image of the same axillary region acquired at 28 min after the injection of nanocages (2 nM, 100 μL) into the forepaw pad of a rat, and the SLN of the rat located at ~2 mm below the skin surface can be obviously identified from this image. In order to evaluate the accumulation of AuNCs in a SLN over time, the changes of PA signal amplitude was calculated versus the time after the injection (Fig. 4C). The PA signal from the SLN started to be detected at about 5 min after the injection, and then increased with time, and finally reached a plateau at ~140min after the injection, indicating the gradual accumulation of AuNCs in the SLN. Figure 4(D–F) shows the depth capability of PA imaging by placing chicken breast tissue on top of the rat skin to demonstrate the feasibility of this method for mapping the SLN of a breast cancer patient. The figure shows three successive PA images with one, two and three layers of chicken breast tissue (each layer was ~10mm thick) placed on the axillary region of the rat. As shown in Fig. 4(F), the SLN as deep as 33 mm below the skin surface could be imaged with good contrast, which is significantly deeper than the ~12mm depth of SLN in humans. By providing additional functionality to the surface of AuNCs, for example, through the modification of targeting ligands to help concentrate their uptake in cancer cells, the AuNCs-based PA imaging system could serve as a promising method for noninvasive SLN identification of metastases.

6. BIOCONJUGATED GOLD NANOCAGES FOR PA IMAGING OF MELANOMAS

One of the biggest advantages of using AuNCs for applications in biomedical imaging lies in the well-established surface chemistry of Au, including the functionalization with a variety of targeting moieties to further enhance the contrast of the targeted region. In a recent study, we successfully demonstrated the use of AuNCs as a contrast agent for quantitative PA imaging of melanomas *in vivo* (46). We evaluated and quantitatively compared contrast enhancement on B16 melanomas provided by both passively and actively targeting AuNCs. In these cases, AuNCs with an edge length of ~46nm were functionalized, respectively, with [Nle^4, D-Phe^7]-α-melanocyte-stimulating hormone ([Nle^4, D-Phe^7]-α-MSH) at the distal ends of thiol-PEG groups (Fig. 5A) for active targeting, and with thiol-PEG groups (Fig. 5E) for passive targeting. [Nle^4, D-Phe^7]-α-MSH can specifically bind to the α-MSH receptors overexpressed on melanomas, thus guiding and enhancing the delivery of AuNCs to melanoma. Following intravenous injection of both types of derivatized AuNCs into two groups of mice, PA imaging of melanoma was performed at a light source of 778 nm, which overlapped with the maximal absorption of AuNCs. Before the injection of AuNCs, control images of melanoma and its surrounding microvasculatures were acquired for each group of mice using different ultrasonic detection frequencies and different light source wavelengths (10 MHz, 778 nm for melanoma imaging; 50 MHz, 570 nm for blood vessel imaging), as shown in Fig. 5(B and F). A series of PA time-course coronal maximum amplitude projection (MAP) images of melanomas for two groups of mice were acquired up to 6h post-injection of 100 |l actively targeting AuNCs (Fig. 5, panels C and D) and passively targeting AuNCs (Fig. 5, panels G and H) at a concentration of 10nM, respectively. As can be visually deduced from these images, the PA signal enhancement within the melanoma (indicated by

Author Manuscript Author Manuscript Author Manuscript Author Manuscript

the golden color) over time was significantly greater for actively targeting [Nle_4, D-Phe^7]-α-MSH-AuNCs than for nonspecifically targeting PEG-AuNCs.

Figure 6(A) shows the statistical data for changes (%) in PA signal amplitude in melanoma as a function of post-injection time. At t = 6h post-injection, the signal enhancement from active targeting was ~300% higher than that from the passive targeting, clearly demonstrating the enhanced uptake and accumulation of AuNCs based on ligand-receptor binding on melanoma cells. Additionally, the trend of PA signal enhancement from the actively and passively targeting AuNCs was significantly different. The PA signal from [Nle^4, D-Phe^7]-α-MSH-AuNCs was rapidly increased in the first 3 h post-injection, and then slowly increased up to 6 h, while the signal from PEG-AuNCs displayed a gradual increase up to 5 h, and then leveled off. Moreover, the active targeting effect was also confirmed by inductively-coupled plasma mass spectrometry (ICP-MS) measurements of Au content in excised tumors (Fig. 6B), revealing that the average number of [Nle^4, D-Phe^7]-α-MSH-AuNCs per tumor mass was 360% higher than the case with PEG-AuNCs.

7. CONCLUDING REMARKS

Photoacoustic imaging is a powerful emerging hybrid modality which provides strong optical absorption contrast with high ultrasonic resolution. The PA signals can be greatly enhanced by exogenous contrast agents, especially by optically tunable Au nanoparticles with strong absorption properties. Gold nanocages are ideal candidates of PA contrast agents because of their large absorption cross sections than commonly used organic dyes and tunable light absorption in the NIR region within the optical window of biological tissues. They have been successfully applied as intravascular contrast agents for PA imaging of cerebral cortex in a rat model to enhance the contrast between blood and the surrounding tissues, allowing more detailed vascular structures to be imaged at greater depths. We have also demonstrated the use of AuNCs as a new class of lymph node tracers for PA imaging of a SLN with a detectable depth as deep as 33 mm, which is adequate for clinical applications. When bioconjugated with tumor-specific ligands, AuNCs were further proven to be an efficient contrast agent for PA imaging of melanomas with both high sensitivity and specificity due to their enhanced accumulation within the tumor. We believe that a combination of AuNCs and PA imaging will provide a very promising platform for early cancer diagnosis, and set the stage for sensitive absorption-based modalities that can offer both anatomical and functional information.

Acknowledgments

This work was supported in part by a research grant (1R01 CA138527) from the NCI, an NIH Director's Pioneer Award (DP OD000798) and startup funds from Washington University in St Louis. This work was performed in part at the Nano Research Facility, a member of the National Nanotechnology Infrastructure Network, which is supported by the National Science Foundation (NSF) under ECS-0335765.

Biography

Younan Xia, received a B.Sc. in Chemical Physics from the University of Science and Technology of China (USTC) in 1987 and then worked as a graduate student for four years at the Fujian Institute of Research on the Structure of Matter, Chinese Academy of Sciences.

Author Manuscript Author Manuscript Author Manuscript Author Manuscript

He came to the USA in 1991, received an M.Sc. in Inorganic Chemistry from the University of Pennsylvania (with the late Professor Alan G. MacDiarmid) in 1993, and a Ph.D. in Physical Chemistry from Harvard University (with Professor George M. Whitesides) in 1996. After a short stint as a postdoctoral fellow in the same group, he started as an Assistant Professor of Chemistry at the University of Washington in Seattle. He was promoted to Associated Professor and Professor in 2002 and 2004, respectively. He moved to Washington University in St Louis in 2007 and is the James M. McKelvey Professor for Advanced Materials in the school of engineering. His research interests include nanostructured materials, nanomedicine, biomaterials, tissue engineering, self-assembly, photonic crystals, colloidal science, surface modification and electrospinning.

REFERENCES

1. Wang LV, Wu H. Biomedical Optics: Principles and Imaging, John Wiley and Sons, Hoboken, NJ, 2007.
2. Grinvald A, Lieke E, Frostig RD, Gilbert CD, Wiesel TN. Functional architecture of cortex revealed by optical imaging of intrinsic signals. Nature 1986; 324: 361–364. [PubMed: 3785405]
3. Rapacholi MH. Essentials of Medical Ultrasound: A Practical Introduction to the Principles, Techniques and Biomedical Applications. Humana: New York, 1982.
4. Wang LV. Multiscale photoacoustic microscopy and computed tomography. Nat Photonics 2009; 3: 503–509. [PubMed: 20161535]
5. Wang XD, Pang YJ, Ku G, Xie XY, Stoica G, Wang LV. Noninvasive laser- induced photoacoustic tomography for structural and functional in vivo imaging of the brain. Nat Biotechnol 2003; 21: 803–806. [PubMed: 12808463]
6. Zhang HF, Maslov K, Stoica G, Wang LV. Functional photoacoustic microscopy for high-resolution and noninvasive in vivo imaging. Nat Biotechnol 2006; 24: 848–851. [PubMed: 16823374]
7. Maslov K, Stoica G, Wang LV. In vivo dark-field reflection-mode photoacoustic microscopy. Opt Lett 2005; 30: 625–627. [PubMed: 15791997]
8. Maslov K, Zhang HF, Hu S, Wang LV. Optical-resolution photoacoustic microscopy for in vivo imaging of single capillaries. Opt Lett 2008; 33: 929–931. [PubMed: 18451942]
9. Song KH, Wang LV. Deep reflection-mode photoacoustic imaging of biological tissue. J Biomed Opt 2007; 12: 060503–1–060503–3.
10. Denk W, Strickler JH, Webb WW. Two-photon laser scanning fluorescence microscopy. Science 1990; 248: 73–76. [PubMed: 2321027]
11. Yang X, Stein EW, Ashkenazi S, Wang LV. Nanoparticles for photoacoustic imaging. Wiley Interdiscip Rev Nanomed Nano-biotechnol 2009; 1: 360–368.
12. Weissleder R A clearer vision for in vivo imaging. Nat Biotechnol 2001; 19: 316–317. [PubMed: 11283581]
13. Murphy CJ, Sau TK, Gole AM, Orendorff CJ, Gao J, Gou L, Hunyadi SE, Li T. Anisotropic metal nanoparticles: synthesis, assembly, and optical applications. J Phys Chem B 2005; 109: 13857–13870 [PubMed: 16852739]
14. Halas NJ. Playing with plasmons: tuning the optical resonant properties of nanoshells. MRS Bull 2005; 30: 362–367.

Author Manuscript Author Manuscript Author Manuscript Author Manuscript

15. Chen JY, Wiley B, Li ZY, Campbell D, Saeki F, Cang H, Au L, Lee J, Li X, Xia Y. Gold nanocages: engineering their structure for biomedical applications. Adv Mater 2005; 17: 2255–2261.
16. Skrabalak SE, Chen J, Au L, Lu X, Li X, Xia Y. Gold nanocages for biomedical applications. Adv Mater 2007; 19: 3177–3184. [PubMed: 18648528]
17. Skrabalak SE, Chen J, Sun Y, Lu X, Au L, Cobley C, Xia Y. Gold nanocages: synthesis, properties, and applications. Acc Chem Res 2008; 41: 1587–1595. [PubMed: 18570442]
18. Chen J, Yang M, Zhang Q, Cho EC, Cobley CM, Claus C, Kim C, Wang LV, Welch MJ, Xia Y. Gold nanocages: a novel class of multifunctional nanomaterials for theranostic applications. Adv Funct Mater 2010; 20: 3684–3694.
19. Skrabalak SE, Au L, Li X, Xia Y. Facile synthesis of Ag nanocubes and Au nanocages. Nat Protoc 2007; 2: 2182–2190. [PubMed: 17853874]
20. Im SH, Lee YT, Wiley BJ, Xia Y. Large-scale synthesis of silver nanocubes: the role of hcl in promoting cube perfection and monodispersity. Angew Chem Int Edn 2005; 44: 2154–2157.
21. Siekkinen AR, McLellan J, Chen J, Xia Y. Rapid synthesis of small silver nanocubes by mediating polyol reduction with a trace amount of sodium sulfide or sodium hydrosulfide. Chem Phys Lett 2006; 432: 491–496. [PubMed: 18496589]
22. Zhang Q, Li W, Moran C, Chen J, Wen L, Xia Y. Seed-mediated synthesis of Ag nanocubes with controllable edge lengths in the range of 30–200 nm and comparison of their optical properties. J Am Chem Soc 2010; 132: 11372–11378. [PubMed: 20698704]
23. Zhang Q, Li W, Wen LP, Chen J, Xia Y. Facile synthesis of Ag nanocubes of 30 to 70 nm in edge length with CF3COOAg as a precursor. Chem A Euro J 2010; 16: 10234–10239.
24. Lampre I, Pernot P, Mostafavi M. Spectral properties and redox potentials of silver atoms complexed by chloride ions in aqueous solution. J Phys Chem B 2000; 104: 6233–6239.
25. Chen J, McLellan JM, Siekkinen A, Xiong Y, Li ZY, Xia Y. Facile synthesis of gold-silver nanocages with controllable pores on the surface. J Am Chem Soc 2006; 128: 14776–14777. [PubMed: 17105266]
26. Ingle JDJ, Crouch SR. Spectrochemical Analysis. Prentice Hall, New Jersey, 1988.
27. Mie G Beiträge zur Optik trü ber Medien, speziell kolloidaler Metallösungen. Ann Phys 1908; 25: 376–455.
28. Draine B, Flatau P. Discrete-dipole approximation for scattering calculations. J Opt Soc Am B 1994; 11: 1491–1499.
29. Cho EC, Kim C, Zhou F, Cobley CM, Song KH, Chen J, Li Z, Wang LV, Xia Y. Measuring the optical absorption cross sections of Au-Ag nanocages and Au nanorods by photoacoustic imaging. J Phys Chem C 2009; 113: 9023–9028.
30. Kim C, Favazza C, Wang LV. In vivo photoacoustic tomography of chemicals: high-resolution functional and molecular optical imaging at new depths. Chem Rev 2010; 110: 2756–2782. [PubMed: 20210338]
31. Hoelen CGA, de Mul FFM, Pongers R, Dekker A. Three-dimensional photoacoustic imaging of blood vessels in tissue. Opt Lett 1998; 23: 648–650. [PubMed: 18084605]
32. Kruger RA, Reinecke DR, Kruger GA. Thermoacoustic computed tomography-technical considerations. Med Phys 1999; 26:1832–1837. [PubMed: 10505871]
33. Xu M, Wang LV. Photoacoustic imaging in biomedicine. Rev Sci Instrum 2006; 77: 1–22.
34. Wang Y, Xie X, Wang X, Ku G, Gill KL, O'Neal DP, Stoica G, Wang LV. Photoacoustic tomography of a nanoshell contrast agent in the in vivo rat brain. Nano Lett 2004; 4: 1689–1692.
35. Yang X, Skrabalak S, Li Z, Xia Y, Wang L. Photoacoustic tomography of a rat cerebral cortex in vivo with Au nanocages as an optical contrast agent. Nano Lett 2007; 7: 3798–3802. [PubMed: 18020475]
36. Song KH, Kim C, Cobley CM, Xia Y, Wang LV. Near-infrared gold nanocages as a new class of tracers for photoacoustic sentinel lymph node mapping on a rat model. Nano Lett 2009; 9: 183–188. [PubMed: 19072058]
37. Tanis PJ, Nieweg OE, Valdes Olmos RA, Th Rutgers EJ, Kroon BB. History of sentinel node and validation of the technique. Breast Cancer Res 2001; 3: 109–112. [PubMed: 11250756]

Author Manuscript Author Manuscript Author Manuscript Author Manuscript

38. Morton DL, Wen DR, Wong JH, Economou JS, Cagle LA, Storm FK, Foshag LJ, Cochran AJ. Intraoperative lymphatic mapping and selective lymphadenectomy: technical details of a new procedure for clinical stage I melanoma. Arch Surg 1992; 127: 392–399. [PubMed: 1558490]

39. Krag DN, Weaver DL, Alex JC, Fairbank JT. Surgical resection and radiolocalization of the sentinel lymph node in breast cancer using a gamma probe. Surg Oncol 1993; 2: 335–340. [PubMed: 8130940]

40. Koyama Y, Talanov VS, Bernardo M, Hama Y, Regino CA, Brechbiel MW, Choyke PL, Kobayashi H. A dendrimer-based nanosized contrast agent dual-labeled for magnetic resonance and optical fluorescence imaging to localize the sentinel lymph node in mice. J Magn Reson Imag 2007; 25: 866–871.

41. Nakajima M, Takeda M, Kobayashi M, Suzuki S, Ohuchi N. Nano-sized fluorescent particles as new tracers for sentinel node detection: experimental model for decision of appropriate size and wavelength. Cancer Sci 2005; 96: 353–356. [PubMed: 15958058]

42. Michel SC, Keller TM, Frohlich JM, Fink D, Caduff R, Seifert B, Marincek B, Kubik-Huch RA. Preoperative breast cancer staging: MR imaging of the axilla with Ul-trasmall superparamagnetic iron oxide enhancement. Radiology 2002; 225: 527–536. [PubMed: 12409591]

43. Torchia MG, Nason R, Danzinger R, Lewis JM, Thliveris JA. Interstitial MR lymphangiography for the detection of sentinel lymph nodes. J Surg Oncol 2001; 78: 151–156. [PubMed: 11745796]

44. Parungo CP, Colson YL, Kim SW, Kim S, Cohn LH, Bawendi MG, Frangioni JV. Sentinel lymph node mapping of the pleural space. Chest 2005; 127: 1799–1804. [PubMed: 15888861]

45. Cuenca AG, Jiang H, Hochwald SN, Delano M, Cance WG, Grobmyer SR. Emerging implications of nanotechnology on cancer diagnostics and therapeutics. Cancer 2006; 107: 459–466. [PubMed: 16795065]

46. Kim C, Cho EC, Chen J, Song KH, Au L, Favazza C, Zhang Q, Cobley CM, Gao F, Xia Y, Wang LV. In vivo molecular photoacoustic tomography of melanomas targeted by bioconjugated gold nanocages. ACS Nano 2010; 4: 4559–4564. [PubMed: 20731439]

Author Manuscript Author Manuscript Author Manuscript Author Manuscript

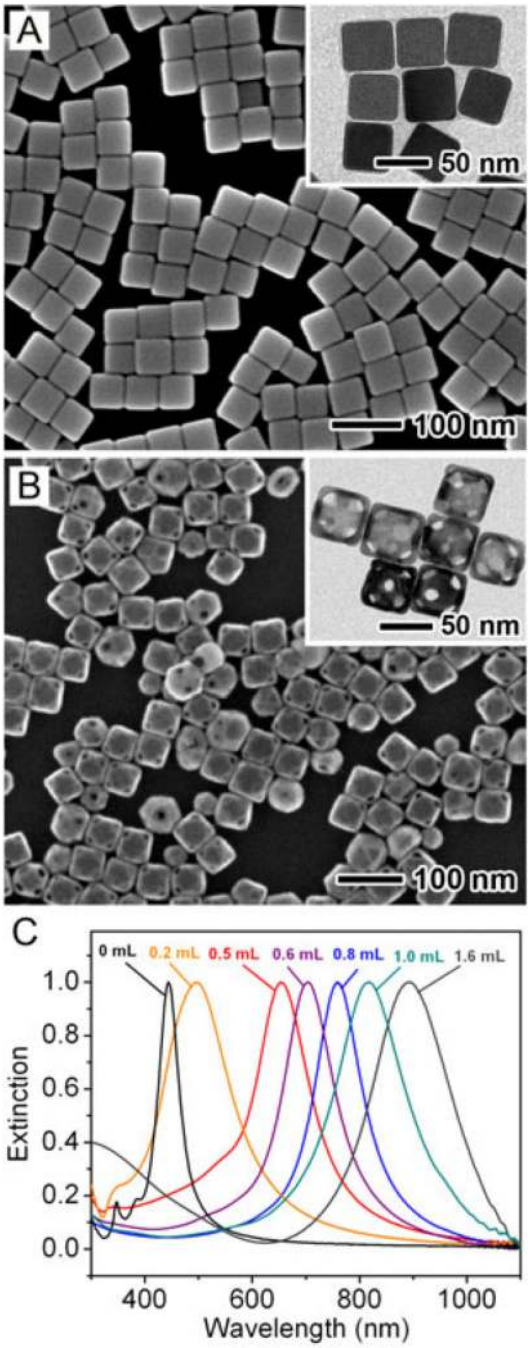

Figure 1.

SEM images of (A) Ag nanocubes and (B) AuNCs. The inset shows the corresponding TEM images of the same sample. (C) UV–vis spectra of the samples obtained by titrating Ag nanocubes with different volumes of 0.1 mM $HAuCl_4$ solution.

Author Manuscript Author Manuscript Author Manuscript Author Manuscript

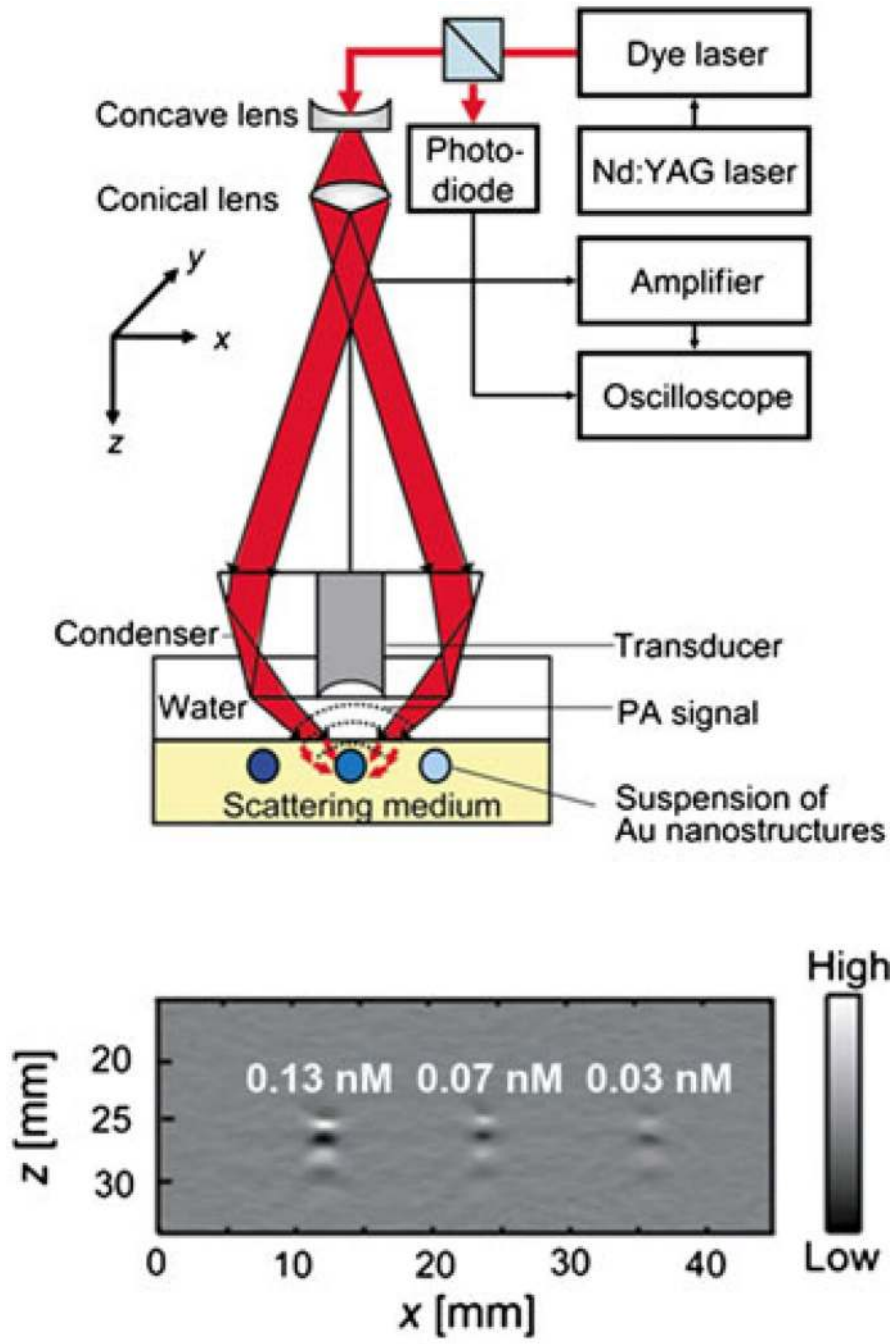

Figure 2.

(top) An experimental setup of a PA imaging system; (bottom) a typical depth-resolved B-scan PA image (*x*-*z* scan) of a suspension of AuNCs at three different concentrations. Reproduced with permission from (29), copyright 2009 American Chemical Society.

Author Manuscript Author Manuscript Author Manuscript Author Manuscript

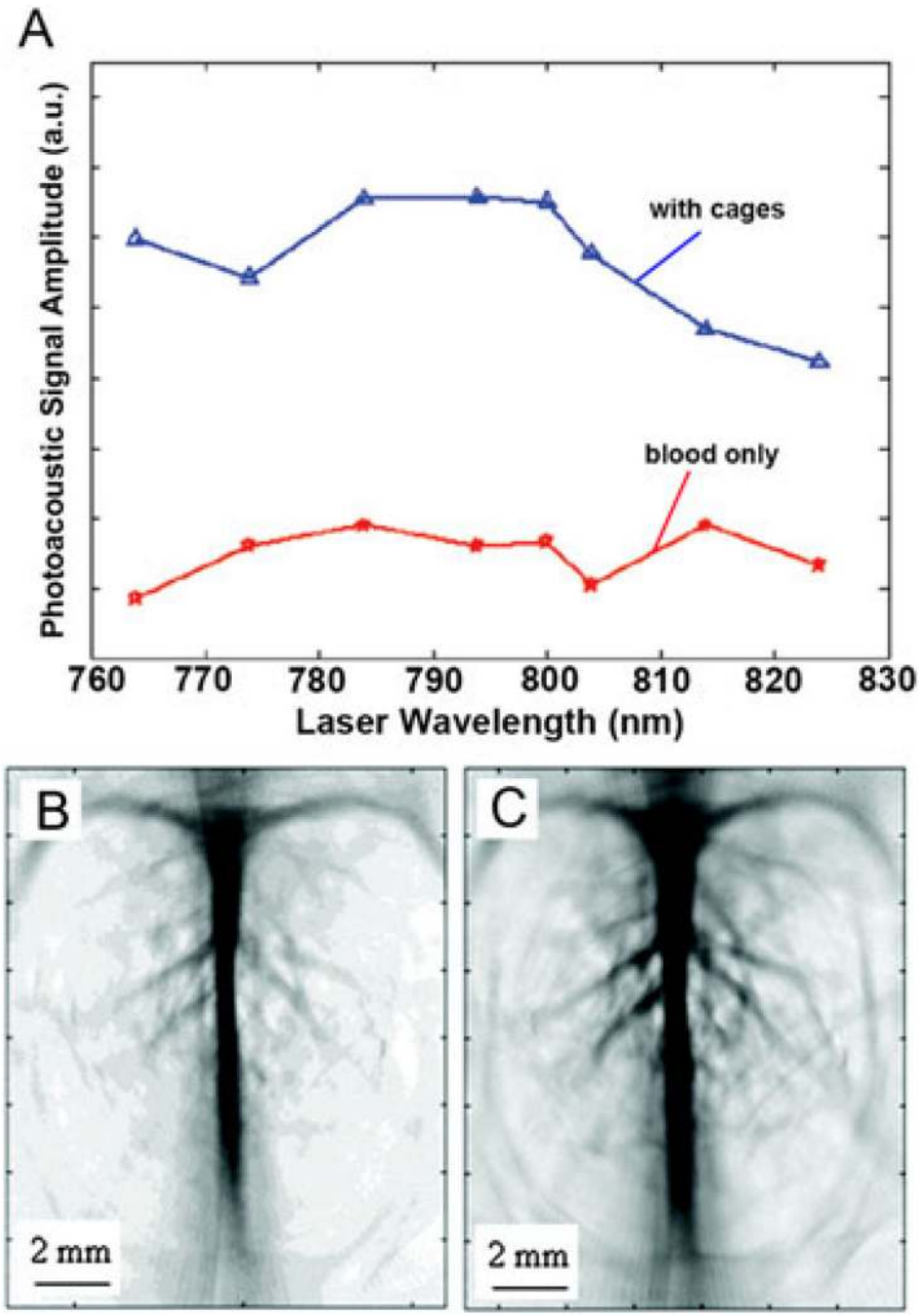

Figure 3.

(A) The measured PA signal amplitude generated with and without AuNCs in rat blood at several wavelengths. Noninvasive PA imaging of a rat's cerebral cortex (B) before the injection of AuNCs and (C) about 2h after the final injection of nanocages, which is the peak enhancement point. Reproduced with permission from (35), copyright 2007 American Chemical Society.

Author Manuscript Author Manuscript Author Manuscript Author Manuscript

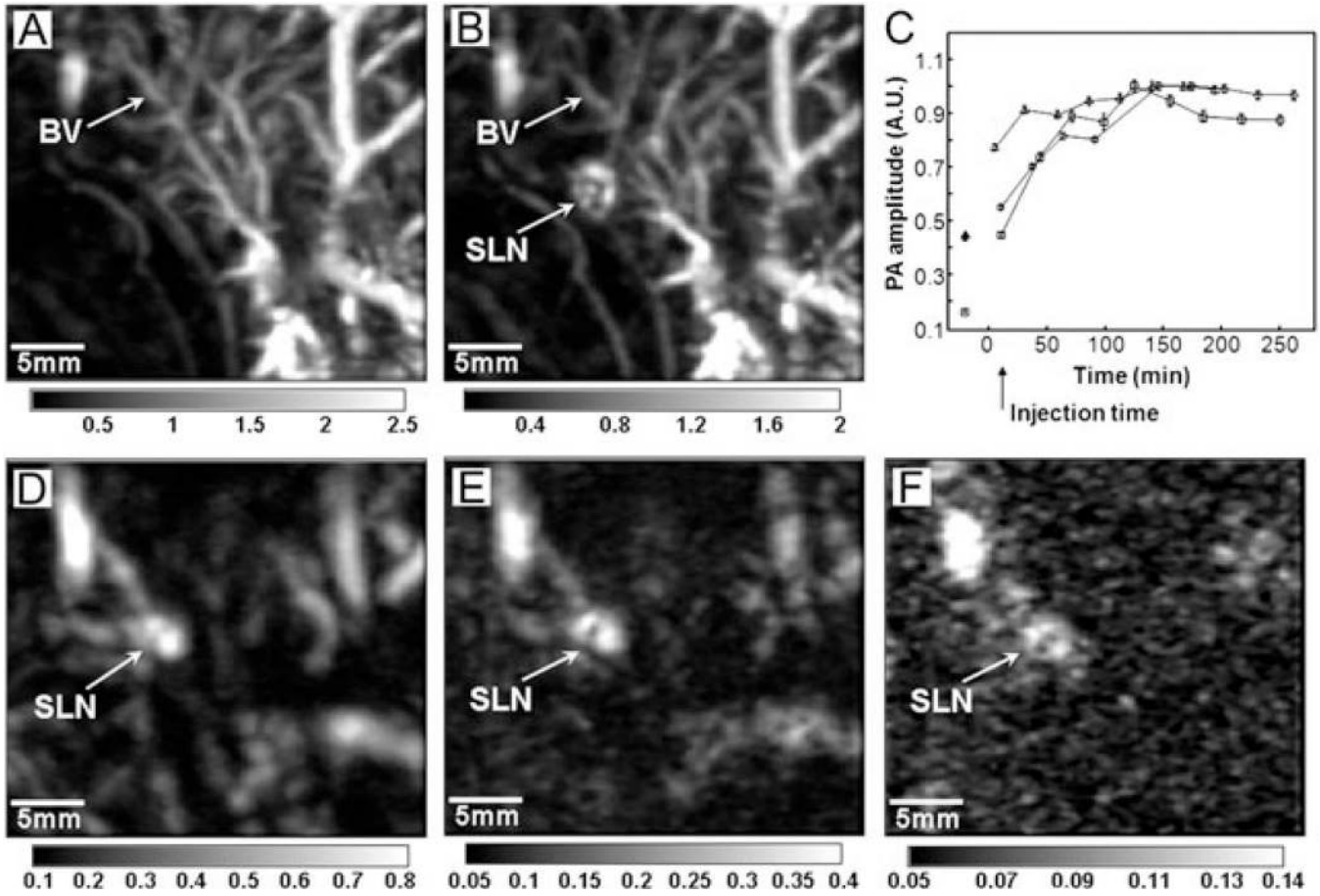

Figure 4.

PA images of the axillary region of a rat taken (A) before and (B) 28 min after the injection of AuNCs. (C) The changes of PA signal amplitude as a function of the post-injection time. After the injection, PA signals increased with time, which means gradual accumulations of the nanocages. (D-F) Depth capability of SLN mapping with AuNCs. The PA images were acquired after the injection of nanocages for: (D) 126 min with a total imaging depth of 10mm by placing a layer of chicken breast tissue on the axillary region; (E) 165 min with a total imaging depth of 21mm by adding another layer of chicken breast tissue; and (F) 226 min with a total imaging depth of 33mm by using three layers of chicken breast tissue. The bars represent the optical absorption. BV, blood vessel. SLN, sentinel lymph node. Reproduced with permission from (36), copyright 2009 American Chemical Society.

Author Manuscript Author Manuscript Author Manuscript Author Manuscript

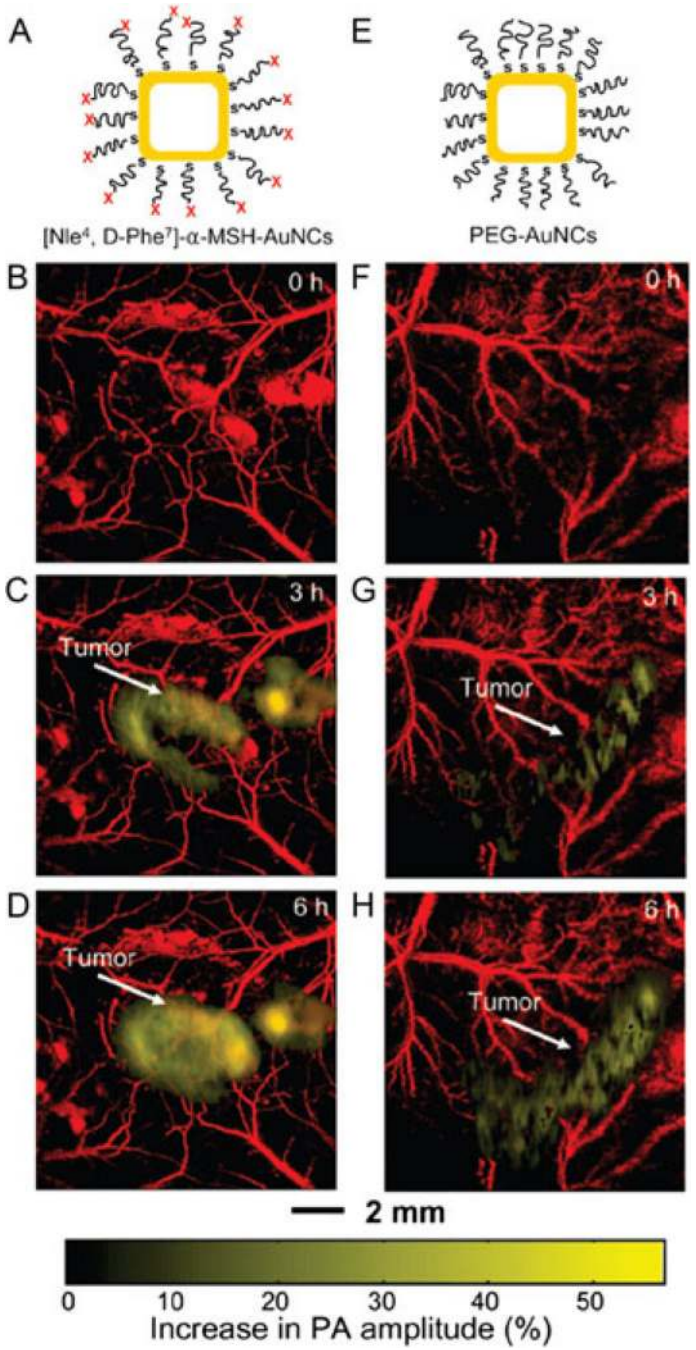

Figure 5.

In vivo noninvasive PA time-course coronal MAP images of B16 melanomas using [Nle^4, D-Phe^7]-α-MSH- and PEG-AuNCs. (A, E) a schematic of the [Nle^4, D-Phe^7]-α-MSH- and PEG-AuNCs. Time-course PA images of the B16 melanomas after intravenous injection with 100 μl of 10 nM (B-D) [Nle^4, D-Phe^7]-α-MSH- and (F-H) PEG-AuNCs through the tail vein. The background vasculature images were obtained using the PA microscope at 570 nm (ultrasonic frequency = 50 MHz), and the melanoma images were obtained using the PA

Author Manuscript Author Manuscript Author Manuscript Author Manuscript

macroscope at 778 nm (ultrasonic frequency = 10 MHz). Reproduced with permission from (46), copyright 2010 American Chemical Society.

Author Manuscript Author Manuscript Author Manuscript Author Manuscript

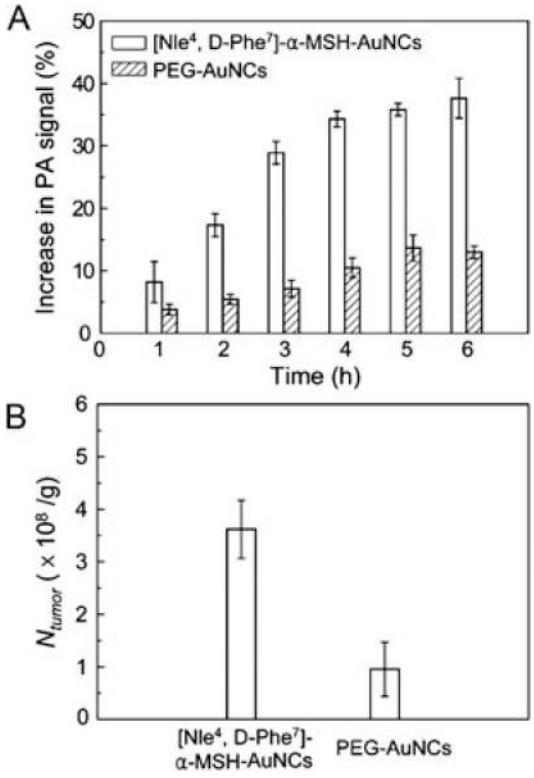

Figure 6.

(A) Increase of PA amplitude in the melanoma tumors after intravenous injection of [[Nle^4, D-Phe^7]-α-MSH-AuNCs and PEG-AuNCs ($n = 4$ mice for each group), respectively, for different periods of time. The PA signals increased up to 38 ± 6% for [Nle^4, D-Phe^7]-α-MSH-AuNCs while the maximum signal increase only reached 13 ± 2% for PEG-AuNCs at a post-injection time of 6h ($p < 0.0001$). (B) The average number of AuNCs accumulated in the melanomas dissected at 6h post-injection for the two types of AuNCs as measured by ICP-MS. Here N_{tumor} denotes the number of AuNCs per unit tumor mass (g). Reproduced with permission from (46), copyright 2010 American Chemical Society.

Author Manuscript Author Manuscript Author Manuscript Author Manuscript

Table 1.

Comparison of the optical cross sections ofAu-based nanostructures obtained experimentally by PA imaging and theoretically by calculation, respectively. Reproduced with permission from (29), copyright 2009 American Chemical Society.

		Cross section (10^{-15} m^2)[a]		σ_a/σ_e
		Extinction (σ_e)	Absorption (σ_a)	
Nanocages (45.0 nm)	Experimental	7.26 ± 0.06	5.96 ± 0.25	0.82 ± 0.04
	Calculated	19.88	16.26	0.82
Nanocages (32.0 nm)	Experimental	2.99 ± 0.04	3.05 ± 0.12	1 ± 0.04
	Calculated	6.39	6.02	0.94
Nanorods (44.0 × 19.8 nm^2)	Experimental	2.16 ±0.02	1.87 ± 0.23	0.87 ± 0.11
	Calculated	2.15	1.83	0.85
Nanospheres (150 nm)	Experimental	145 ± 14.76	_[b]	—
	Calculated	99.96	5.73	0.056

[a] All the values were obtained at 638 nm.

[b] Not detected with PA imaging.